

Droplet bounce simulations and air pressure effects on the deformation of pre-impact droplets, using a boundary element method

Hongbok Park^a, Sam S. Yoon^{b,*}, Richard A. Jepsen^c, Stephen D. Heister^d, Ho Y. Kim^b

^aADD, 3-Hyun-3, 111 Sunam-Dong, Yuseong-Gu, Taejon 305-152, Republic of Korea

^bDepartment of Mechanical Engineering, Korea University, Anamdong, 5-Ga, Sungbukgu, Seoul 136-713, Republic of Korea

^cMechanical Environment, Sandia National Laboratory, P. O. Box 5800, Albuquerque, NM 87185-1135, USA

^dSchool of Aeronautics and Astronautics, Purdue University, West Lafayette, IN 47907, USA

Received 11 December 2006; accepted 19 July 2007

Available online 30 August 2007

Abstract

An inviscid axisymmetric model capable of predicting both droplet bounce and the detailed pre-impact motion that is influenced by ambient pressure has been developed using a boundary element method (BEM). Previous simulations could not accurately describe the effect of the gas compressed between a falling droplet and the impacting substrate because most droplet impact simulations assumed that the droplet was already in contact with the impacting substrate at the beginning of the simulation. To properly account for the surrounding gas, the simulation must begin when the droplet is released from a certain height. High pressures are computed in the gas phase in the region between the droplet and the impact surface at instances just prior to impact. This simulation shows that the droplet retains its spherical shape when the surface tension energy is dominant over the dissipative energy. When the Weber number is increased, the droplet's surface structure is highly deformed due to the presence of capillary waves and, consequently, a pyramidal surface structure is formed. This phenomenon was verified experimentally. Parametric studies using our model include the pre-impact behavior that varies as a function of the Weber number and the surrounding gas pressure.

© 2007 Elsevier Ltd. All rights reserved.

Keywords: Droplet impact; Compressed gas; Splashing; Two-phase flow; Bouncing droplet

1. Introduction

Droplet impact phenomena are readily encountered in raindrop impact and in numerous industrial applications such as inkjet printing, painting, spray-wall impact within IC-engines, and fire suppression sprays. As shown in classical experiments [1,2], a droplet will stick to the impacting substrate when the droplet surface tension energy is not high enough to overcome the droplet's dissipative energy [3]. Upon sticking, the droplet spreads radially and forms a toroidal ring when it has a relatively low Weber number. At an intermediate Weber number, an azimuthal instability develops and forms “fingers” at the rim of the spreading ring. If the Weber number is

increased, the droplet “splashes” upon contact with the substrate and the fingers shed additional individual drops.

There are two schools of thought as to the reason of the fundamental instability of the splashing and the subsequent finger formation: one theory is based on the Rayleigh–Taylor-type buoyancy driven instability and the other presumes a Kelvin–Helmholtz-type shear layer driven instability [4]. The debate about which instability is the primary source for causing the splashing and the finger formation is a subject that needs further scrutiny.

The debate on whether or not liquid viscosity plays an important role for the formation of fingers is another idea that further complicates this subject. Impacting substrate conditions such as porosity, roughness, and temperature are also known to play a prominent role during droplet impact. All of the aforementioned studies of a single droplet impact have been used as the basis for the polydisperse spray simulation. Sivakumar and Tropea [5],

*Corresponding author. Tel.: +82 2 3290 3376; fax: +82 2 926 9290.

E-mail address: skyoona@korea.ac.kr (S.S. Yoon).

however, concluded that using the results from a single droplet should not be extended to the model for the spray simulation because of the interaction between multiple droplets. In other words, the results from a single droplet could not be linearly extrapolated to accurately explain what happens within a spray that is comprised of many droplets.

While one may be astounded and puzzled by the magnitude and complexity of liquid impact physics, one thing is clear: the effect of gas pressure on splashing is conspicuously manifested when the gas pressure is varied from 100 to 17 kPa as shown in Fig. 1 of Xu et al.'s experiment [6] and in the induced vortex rollup motion of gas due to a falling droplet as shown in Fig. 2 of our experiment. We attempt to address this gas pressure effect on the pre-impact condition of a falling droplet using the BEM. The boundary element technique is ideal for this type of problem due to the established accuracy of the methodology for highly deformed free-surface problems.

As mentioned earlier, there are numerous parameters, such as liquid viscosity, surface roughness, porosity and temperature, which can substantially change the spreading behavior of a droplet after impact. The objective of this study is to assess contributions of air to the pre-impact

deformation process using BEM. It is noted that the current model is not capable of simulating the actual splashing that occurs after impact. We also note that the Kelvin–Helmholtz shear layer driven instability plays a major role in causing the initial disturbance, which we believe is capable of causing the splashing and the subsequent finger formation at the spreading edge. Allen [7] claimed that the accelerating light air against the decelerating heavy liquid of a “spreading” droplet poses the unstable interface of the Rayleigh–Taylor instability. Allen [7] did not consider that the case of a “falling” droplet was not only subject to the Rayleigh–Taylor instability, but also to the Kelvin–Helmholtz instability. The inviscid assumption applied in the BEM approach should be valid since the Kelvin–Helmholtz/Rayleigh–Taylor debate over the dominant instability mechanism in causing splash are both based on the inviscid assumption at an infinitesimally small length scale: $\lambda \rightarrow 0$.

Furthermore, the current modeling effort is unique in that the droplet falls from a certain distance above the impacting wall. Other similar numerical efforts [8–15] begin their simulation at the time when the impacting droplet comes in contact with the wall and thus, the compressed air effect due to the falling droplet could not be resolved. Certainly, the gas effect on the droplet's initial disturbance and subsequent splashing and fingering is a new phenomenon that was recently discovered by Nagel's group. To the authors' knowledge, there has been no relevant numerical modeling effort found in literature; therefore, our current modeling results are merited.

To validate the modeling results, we considered the “non-splashing” case of a spreading droplet. The maximum spreading radius data will be quantitatively compared to the existing experimental data of Mao et al. [16] and with the correlation proposed by Aziz and Chandra [3]. The shapes of the rebounding droplet were then quantitatively compared to the photographic images of the experiments. After the validation studies, the deformed shape and induced slip velocities of a liquid droplet were presented at various atmospheric pressures.

2. Modeling

2.1. Two-phase flow modeling

Heister [17] provides a complete description of the basic modeling elements involved with a BEM application to

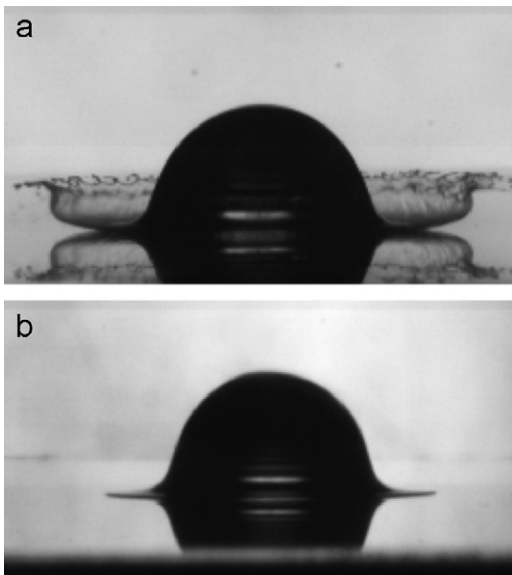


Fig. 1. Xu et al.'s [6] experiment. When the gas pressure is reduced, splashing is prevented. Reprinted under the permission of Prof. Nagel of University of Chicago.



Fig. 2. Development of the vortex rollup motion while gas being compressed due to a falling drop. Photographs are from our ongoing experiment.

two-phase flows. For brevity, only highlights will be presented. In an inviscid, incompressible, axisymmetric flow, it is presumed that the flow dynamics are governed by Laplace's equation: $\nabla^2\phi = 0$. The boundary element method (BEM) utilizes an integral representation of this equation to provide a connection between the values on the boundary, the local geometry, and the local velocity normal to the boundary, $q = \partial\phi/\partial n$, as follows:

$$\alpha\phi(\vec{r}_i) + \int_S \left[\phi \frac{\partial G}{\partial n} - qG \right] ds = 0, \quad (1)$$

where $\phi(\vec{r}_i)$ is the value of the potential at a point \vec{r}_i , S is the boundary of the domain, α is the singular contribution when the integral path passes over the "base point", and G is the free-space Green's function corresponding to Laplace's equation. For an axisymmetric domain, the free-space Green's function can be expressed in terms of elliptic integrals of the first and second kinds and is a function solely of the instantaneous surface geometry. For this reason, a discrete representation of Eq. (1) can be cast as a linear system of equations relating local ϕ and q values. In the discretization, both ϕ and q are assumed to vary linearly along each element thereby providing a formal second-order accuracy for the method. Since the resulting integrals do not have exact solutions in this case, a 4-point Gaussian quadrature is used to maintain a high accuracy of integration and to preserve the second-order accuracy overall.

While this governing equation is linear, non-linearity in these free-surface problems enters through the boundary condition at the interface. The unsteady Bernoulli equation provides a connection between the local velocity potential and the surface shape at any instant in time. Prior formulations [17,18] have provided a derivation of this result that is suitable for implementation into a Lagrangian surface tracking environment. The dimensionless form of the unsteady Bernoulli equation for a liquid surface is given below. The three characteristic parameters in these equations are droplet radius (a), the impact speed (U), and the liquid density (ρ_l):

$$\frac{\partial\phi}{\partial t} + \frac{1}{2}|\nabla\phi|^2 + P_{\text{gas}} + \frac{\kappa}{We} - \frac{Bo}{We}z = 0, \quad (2)$$

where ϕ is the velocity potential, κ is the local surface curvature. The Weber and Bond numbers are defined by $We = \rho_l U^2 a / \sigma$ and $Bo = \rho_l g a^2 / \sigma$, respectively, where σ is the fluid surface tension. The Eulerian–Lagrangian transformation for surface nodes moving with the velocity of the liquid is

$$\frac{D(\cdot)}{Dt} = \frac{\partial(\cdot)}{\partial t} + \nabla\phi \nabla(\cdot), \quad (3)$$

where D/Dt denotes a material or Lagrangian derivative. Using this transformation the dimensionless Bernoulli equation at the free surface of the liquid becomes

$$\frac{D\phi}{Dt} = \frac{1}{2}|\nabla\phi|^2 - P_g - \frac{\kappa}{We} + \frac{Bo}{We}z. \quad (4)$$

Physically, this Bernoulli equation is in a Lagrangian form that is suitable for fluid elements moving with the local velocity of the free surface. Eq. (4) includes the effects from dynamic pressure, local gas-phase pressure, capillary pressure, and hydrostatic pressure, respectively.

An analogous treatment for the gas phase gives

$$\varepsilon \frac{D\phi_g}{Dt} = \varepsilon \nabla\phi \nabla\phi_g - \frac{\varepsilon}{2} |\nabla\phi_g|^2 - P_{\text{gas}}, \quad (5)$$

where ε is the gas/liquid density ratio ($\varepsilon = \rho_g/\rho_l$). Mathematically, Eqs. (4) and (5) provide a system of relations to describe the evolution of the free surface. These nonlinear boundary conditions are coupled at the interface between the gas and liquid phases. Since the gas nodes on the interface are set to be coincident with the nodes in the liquid phase, the liquid velocity is used to advect both sets of nodes on the interface. The kinematic boundary condition provides the necessary relationships to integrate this motion:

$$\begin{aligned} \frac{Dz}{Dt} &= u = \frac{\partial\phi}{\partial s} \cos\beta - q \sin\beta, \\ \frac{Dr}{Dt} &= v = \frac{\partial\phi}{\partial s} \sin\beta + q \cos\beta, \end{aligned} \quad (6)$$

where β is the local slope of the wave with respect to the horizontal direction and r and z are the radial and axial coordinates, respectively. Eqs. (4)–(6) are integrated in time using the fourth-order Runge–Kutta scheme to provide the evolution of the velocity potential and the motion of the free surface. For long integrations or resolution of highly distorted surfaces, points on the free surface will tend to bunch in regions of higher curvature as a result of the free-surface motion. For this reason, the points on the free surface are redistributed at each time step using a cubic spline fitting of the instantaneous shape. Fourth-order accuracy is also employed in computing all surface derivatives in order to maximize the accuracy of the surface evolution method. The Laplace equation is solved to update velocities and the process continues for a set period.

2.2. Computational details

A schematic of the computational domain for the drop impact problem is shown in Fig. 3. The outer boundary for the gas domain, which is fixed in space, is large enough to encompass the liquid droplet for the entire duration of the calculation. If this outer boundary is placed far enough from the liquid domain, the influence of the outer boundary condition on the flow field around a liquid droplet is negligible. Therefore, a coarse grid can be used along this outer boundary. The impacting wall, the bottom wall of this schematic, is considered to be a smooth dry wall. This boundary condition can be treated simply as a no flux condition through the wall, i.e., $q = 0$. Note here that the dissipative energy induced by the substrate's roughness is not taken into account in this model. The

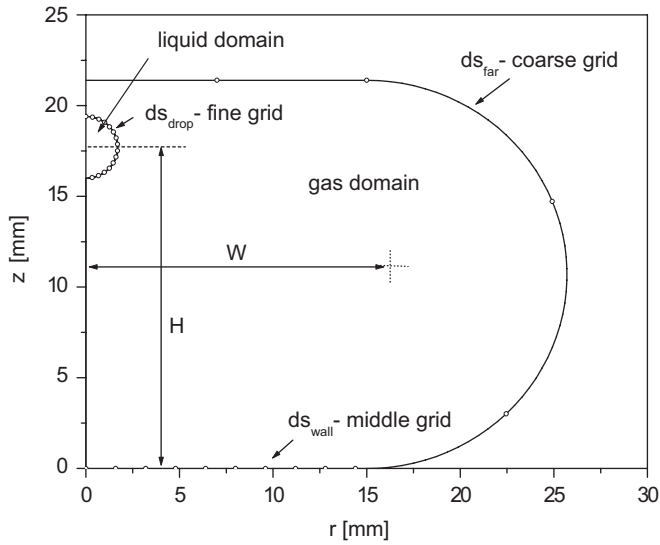


Fig. 3. A schematic for the computational domain of the two-phase flow. A liquid droplet is released at the height of H (axially) within the gas domain having the width of W in the radial direction.

computational time is heavily dependent on the grid size of this outer boundary because the outer boundary is relatively long. The high grid resolution applied around the liquid droplet also adds much computational time.

The appropriate initial grid spacing for the inner/outer boundary was found via a grid convergence study. Typical grid spacing for the liquid droplet surface (ds_{drop}) and for the wall boundary (ds_{wall}) with respect to the droplet radius were found to be $ds_{\text{drop}} = 0.02$ and $ds_{\text{wall}} = 0.04$, respectively. The grid spacing for the outer boundary (ds_{far}) was set to $ds_{\text{far}} = 5ds_{\text{wall}}$. A typical calculation involved about 250 nodes along the liquid droplet and about 400 nodes along the outer boundary.

The following parameters and the fluid properties were set to be consistent with those of the experiment conducted by Xu et al. [6]: the radius of the alcohol droplet was set at $a = 1.7$ mm and the droplet impact velocity was $U = 3.74$ m/s. The alcohol density and its surface tension were $\rho_1 = 789$ kg/m³ and $\sigma = 0.0224$ kg/s², respectively. The applied Weber and Bond numbers were, therefore, $We = \rho_1 U^2 a / \sigma = 837.9$ and $Bo = \rho_1 g a^2 / \sigma = 0.998$, respectively. The density ratio was set at $\varepsilon = \rho_g / \rho_1 = 0.00158$. The dimensionless environmental gas pressure is defined by $P_{\text{env}}^* = P_{\text{atm}} / U^2 \rho_1$ and, thus, its numerical value is approximately $P_{\text{env}}^* \approx 9$ under the given atmospheric pressure of $P_{\text{atm}} = 101$ kPa or 1 atm.

The liquid droplet was initially located one droplet diameter away from the upper outer boundary in our simulation as indicated in Fig. 3. The droplet center was initially located $17a$ from the bottom substrate's wall with a pressure of 1 atm. Numerical studies indicated that this starting condition was sufficiently far from the wall to introduce minimal gas pressure buildup due to the proximity of the wall. A series of convergence tests for the grid spacing and the integration time were performed.

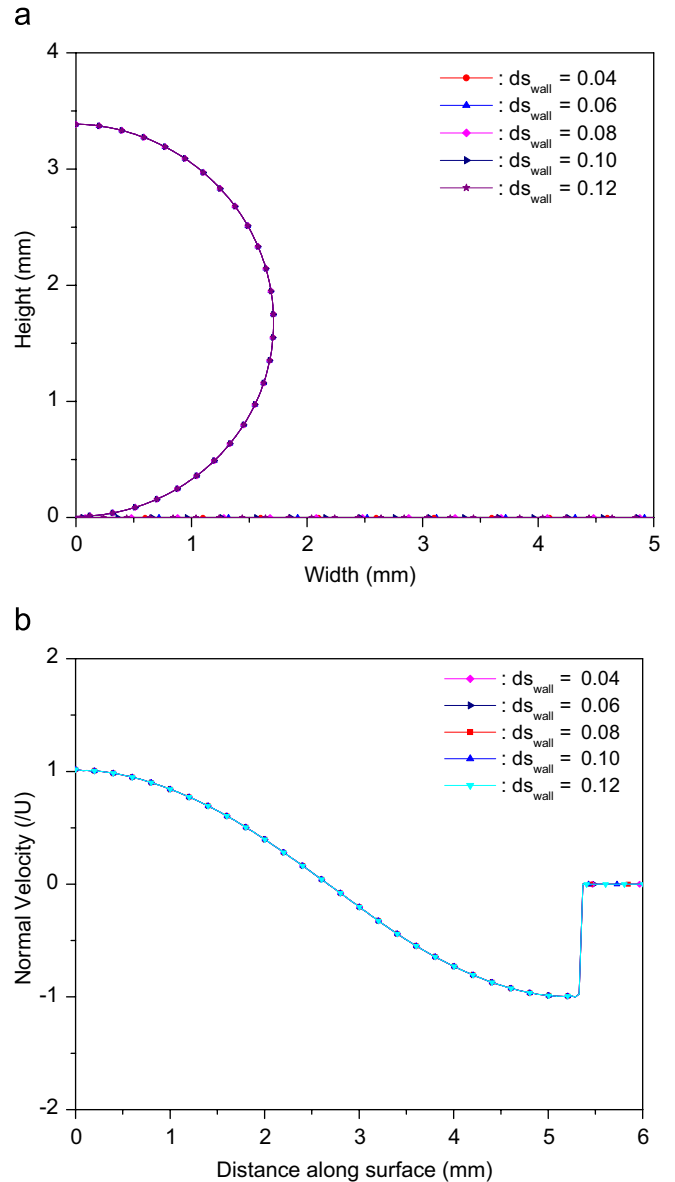


Fig. 4. Droplet shape and gas normal velocity along the droplet's surface for various ds_{wall} .

Fig. 4 shows the droplet's shapes and the normal velocities with the grid size of the outer boundary at the instance of impact. As shown in Fig. 4, there is a good collapse of data for the various grid sizes. These converged results are an indication of the solution's independence of the grid spacing, ds_{wall} . It should be mentioned that the results were also independent of the various widths of the gas domain (see the definition of W in Fig. 3). The results are so nearly identical that most of the data overlaps. These results lead us to conclude that we could use a coarser grid and a smaller gas domain to expedite the computational time. However, it is important that the grid size be small enough to capture the detailed physics at the droplet surface that is in contact with the substrate. Moreover, one should envision the expansion of the spreading droplet, in

which case a fine grid spacing is necessary. In order to minimize such inaccuracies, we have chosen a large gas domain size and a fine grid spacing as follows: $W = 15a$, $H = 37a$, and $ds_{\text{wall}} = 0.04$, where H represents the height measured from the initial location of the droplet to the bottom of the substrate. A typical calculation takes about 5 days using a 1-GHz CPU machine.

3. Results and discussion

3.1. Model validation

It is essential to verify and validate the capability of the current model. To validate, we have compared the BEM model results to experimental data as well as other models that were previously validated by other authors.

First, the model by Aziz and Chandra [3] is introduced by balancing the incoming surface and kinetic energy with the post-impact surface, kinetic, and dissipative energy. The following equation is known to be applicable for the case of isothermal droplet impact:

$$\beta_{\max} = \sqrt{\frac{We_D + 12}{3(1 - \cos \theta_a) + 4(We_D/\sqrt{Re})}}, \quad (7)$$

where β_{\max} is defined as the ratio of the maximum diameter to the initial diameter of an impacting droplet ($\beta_{\max} = D_{\max}/D$). Here, θ_a is referred to as the advancing angle, whose value is approximately $\sim 110^\circ$ [11], but the value is replaced with the measurement by Mao et al. [16], $\theta_a = 97^\circ$ for consistent comparison. It is noted that β_{\max} is not significantly affected by the variation of θ_a within $\pm 20^\circ$. Also note that the Weber number here is defined using the droplet diameter, not the radius: $We_D = \rho_1 U^2 D / \sigma = 2We$, where $D = 2a$. The Reynolds number is defined by: $Re = UD/\nu_1$.

The model suggested by Gong [19] used a slightly different approach in evaluating the viscous dissipation work compared to that of Pasandideh-Fard et al. [11]. Gong [19] considered the effect of the thickness of the boundary layer and assumed an ‘‘ice hockey puck’’ deformation of the liquid droplet upon impact. Gong’s proposed model is as follows:

$$3 \frac{We_D}{\sqrt{Re}} \beta_{\max}^4 + 30(1 - \cos \theta_a) \beta_{\max}^2 + \frac{80}{\beta_{\max}} = 10We_D + 120. \quad (8)$$

Eq. (8) is solved using Newton’s method with a given Weber and Reynolds number. Eqs. (7) and (8) are solved for the case of a water droplet whose diameter is $D = 3.4\text{ mm}$. The range of the Weber number is $0.1 < We_D < 1000$. These results were obtained and then plotted against the current BEM results in Fig. 5. As shown, the BEM predictions are in quantitative agreement with the previously obtained experimental data for $1 < We < 100$. It is noteworthy to mention that the trends predicted from the BEM prediction are comparable to the model suggested by

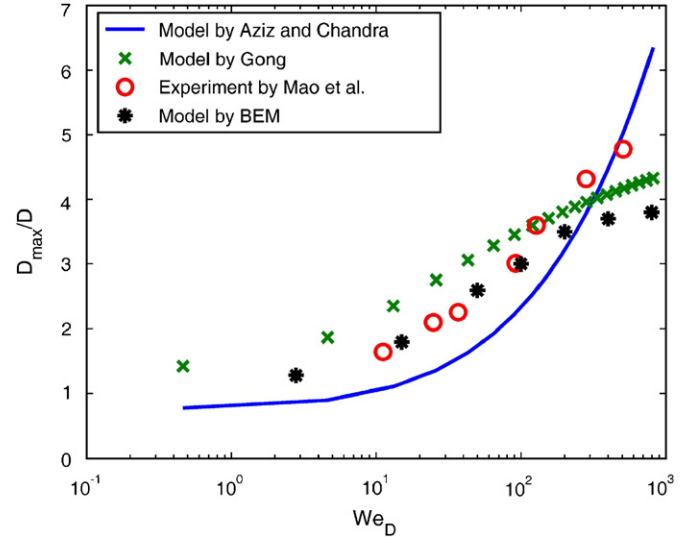


Fig. 5. The maximum spreading diameter comparisons; the data were obtained using various analytical models and experiment.

Gong [19]. At a relatively high Weber number, the maximum spreading diameter reaches a somewhat limiting value. The value of β_{\max} does not show any substantial increase as the Weber increases toward ~ 1000 ; a similar decaying behavior in the spreading diameter rate is shown by Gong’s model [19]. On the other hand, Aziz and Chandra’s [3] model shows a substantial increase in β_{\max} as the Weber number increases. It should be mentioned that Eq. (7) of Aziz and Chandra [3] is not applicable for a Weber number smaller than 10. As shown in Fig. 5, the value of β_{\max} is less than 1 when $We < 10$, a case that is not physically possible.

Fig. 6 shows a qualitative comparison of the model result with the experiment of Xu et al. [6] for an alcohol droplet impinging on a smooth dry substrate at a low atmospheric condition, $P_{\text{atm}} = 17.2\text{ kPa}$ (nearly a vacuum). The simulation of the droplet hitting and the subsequent spreading is qualitatively similar to the experimental result. Since the BEM predictive capability is well validated in this section, we move on to investigating the droplet bounce (or rebound) and the pre-impact condition of the droplet at various atmospheric pressures.

3.2. Droplet bounce in vacuum

Fig. 7 shows the bouncing motion of a falling droplet in a vacuum environment where the surface tension is relatively large. This simulation was performed for Yoon et al.’s experimental conditions for big balloon splashing [20], where the typical value of the surface tension is extremely high. In this case, the droplet retains a spherical or oval shape. The size and the impact velocity of the big water balloon were 0.1 m in radius and 10 m/s, respectively. When the surface tension was decreased (an increase in We is a decrease in surface tension) as in Fig. 8, the droplet behaves like a balloon containing water. If the surface

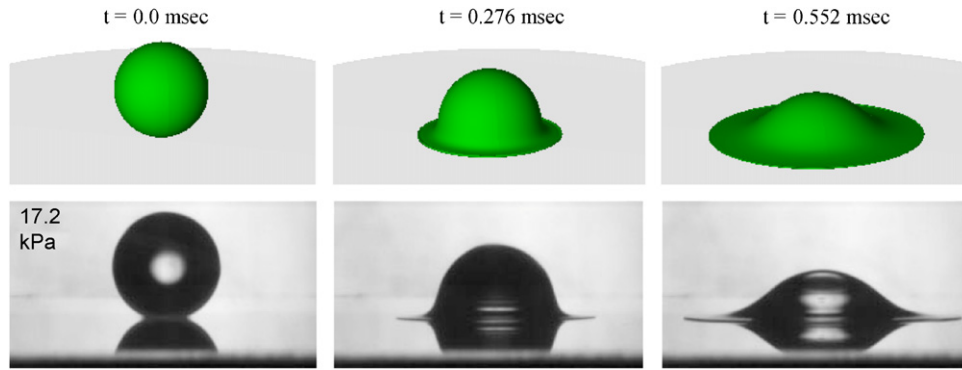


Fig. 6. The comparison of the droplet shape between the modeling results and the experimental images of Xu et al. [6] at $P_{\text{atm}} = 17.2 \text{ kPa}$. Note that the splashing does not occur at this relatively low atmospheric pressure.

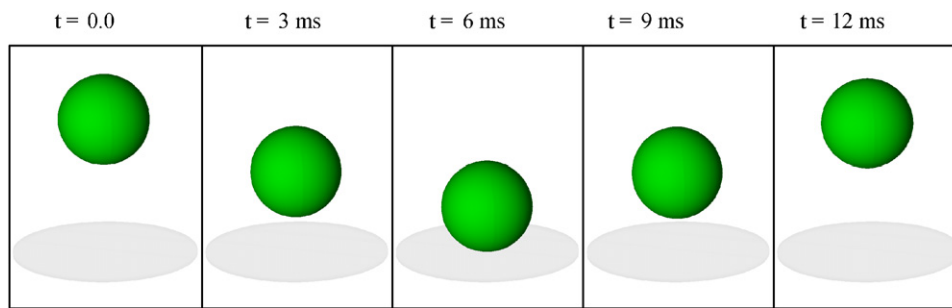


Fig. 7. Bouncing balloon of Yoon et al. [20] retains its spherical shape without any deformation. The estimated Weber number is approximately $We = 0.014$.

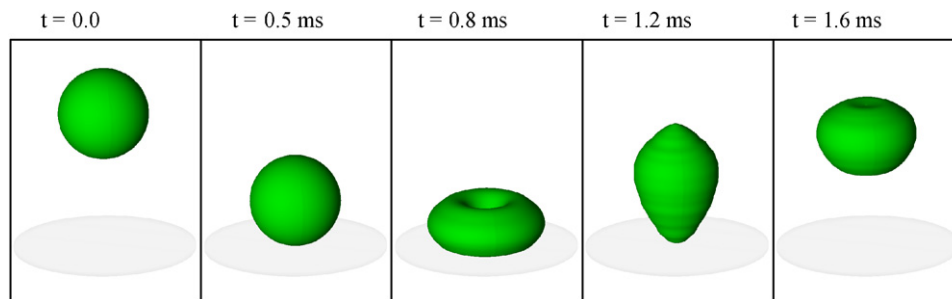


Fig. 8. Deformed bouncing droplet under vacuum condition at $We = 1.4$.

tension is lowered, the droplet will not retain its spherical shape and the induced capillary waves appear at the droplet surface. The waves (or ripples) are sometimes described as pyramids that are formed during the regime where $We Ca < 1$ as proposed by Renardy et al. [21]. Here, Ca represents the capillary number defined by $Ca = \mu U / \sigma$ and whose value is less than unity. Thus, the flow regime of our experiment fell into the category proposed by Renardy et al. [21].

In Fig. 9, a typical bouncing droplet is simulated and compared with the experimental image. In Fig. 10 the “doughnut-shaped” droplet with an erupting jet at the center is simulated and compared with the experimental image. This jet eruption is produced because of the cavity

formed at the droplet’s top center during the surface deformation and the subsequent wave movement during impact. This wave movement is further manifested in our own experimental images as shown in Fig. 11. The capillary waves can be seen traveling along the droplet’s surface and the wave amplitude reduces in size eventually disappearing at the droplet’s top.

3.3. Effect of gas presence

The effect of environmental gas was investigated in Xu et al.’s [6] experiment where the size of the alcohol droplet was 1.7 mm in radius and its impact velocity was 3.74 m/s. In Section 3.2, we attempted to show, computationally, the

effect of gas presence, which was compellingly evidenced by the experiment conducted by Xu et al. [6].

The droplet’s shape and its pressure distribution along its surface at the instance of impact within a gas pressure environment of 1 atm are shown in Fig. 12. Note that the droplet is released from far upstream rather than assuming that the droplet is already in contact with the impacting substrate at $t = 0$. This properly takes into account the gas pressure variations beneath the droplet. It can be observed in Fig. 12(a) that our model predicts the slight deformation of the falling droplet just prior to impact. In Fig. 12(b), the increase in gas pressure along the droplet surface is shown. Note that the x -axis represents the length of the semi-perimeter of the droplet circle so that $s = 0$ represents the droplet’s top while $s = \pi a \approx 5.34\text{mm}$ represents the droplet’s bottom that is in contact with the substrate. The gas pressure peaks at around $|\Delta P_{\text{gas}}| = |P_{\text{gas}} - P_{\text{env}}| \approx 0.013\text{ atm}$, where $P_{\text{env}} = 1\text{ atm}$ and the moderate increase of the gas pressure due to the falling droplet lies with $\sim 1.3\%$.

As for the gas velocity in Fig. 13, the maximum horizontal velocity ($\sim 4.5U\text{m/s}$) is larger than the vertical velocity ($\sim 1.75U\text{m/s}$). This result is in good agreement

with the experimental observation [20,22]. The gas was accelerated because its volume was squeezed between the falling droplet and the substrate. In this case, the droplet’s surface is susceptible to the Kelvin–Helmholtz instability, which may be the fundamental cause of splashing. In Fig. 13(a), the gas near the substrate is also escaping with nearly the same velocity as the velocity along the droplet’s surface. The high peak region is located near the collapsed region within the droplet’s radius and is noted with the symbol “ a ” in Fig. 13(a). It is noteworthy that the gas velocity profile is nearly symmetrical at the contact point because the droplet surface at that point is flat and its tangent is parallel to the substrate’s wall. However, the

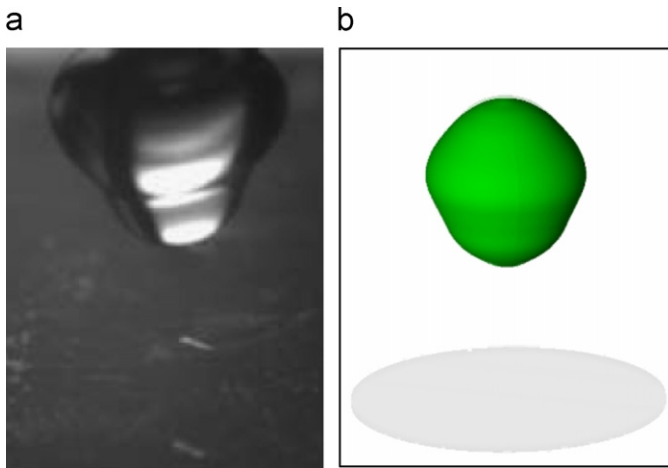


Fig. 9. Typical rebounding droplets. (a) Experimental image by Renardy et al. [21] is reprinted under the permission of Journal of Fluid Mechanics. (b) Model prediction.

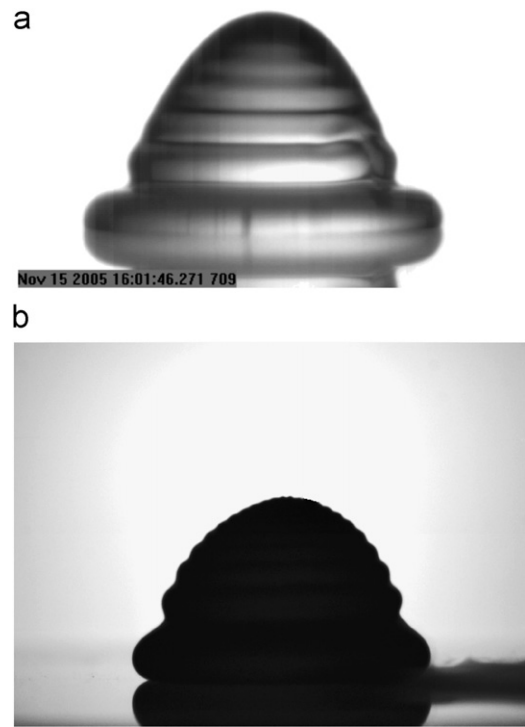


Fig. 11. Typical pyramidal shape of droplets formed on plexiglas. Photographs are from our ongoing experiment. (a) Water droplet. (b) Balloon containing water.

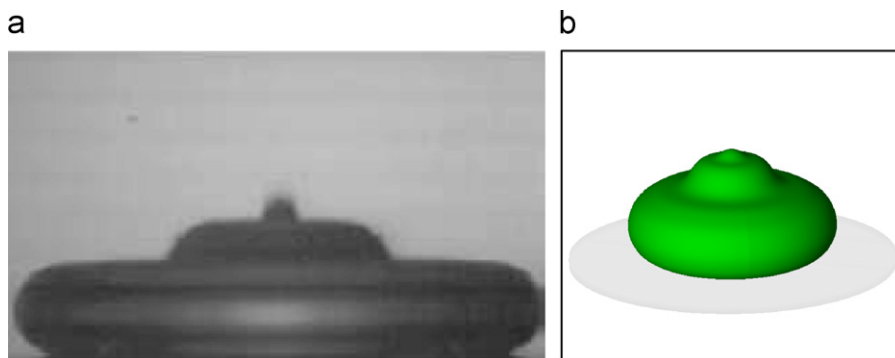


Fig. 10. Appearance of the pyramidal surface structure when $We Ca < 1$. (a) Experiment image by Renardy et al. [21] is reprinted under the permission of Journal of Fluid Mechanics. (b) Modeling prediction.

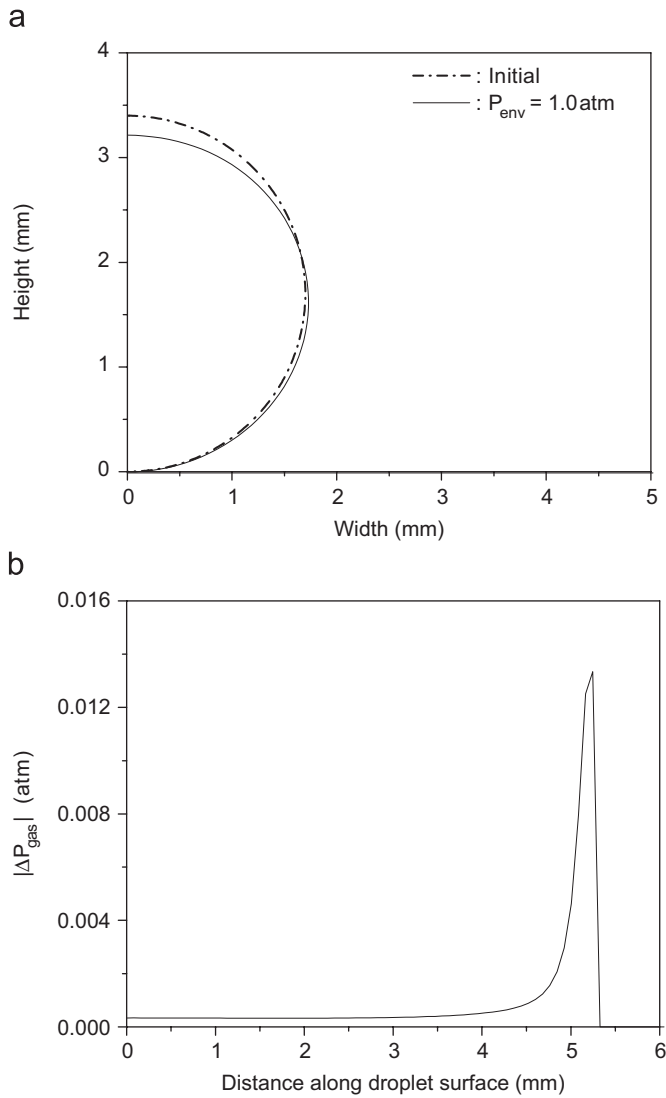


Fig. 12. The ambient pressure effect on (a) the droplet shape and (b) the pressure distribution along the droplet surface during impact.

symmetry disappears when it is farther from the contact point as shown in Fig. 13(a). This asymmetry is because the droplet surface’s tangent is no longer parallel to the substrate’s wall. In Fig. 13(b) the vertical gas velocity also reaches its maximum value ($\sim 1.75U \text{ m/s}$) near the droplet’s bottom. This vertical component of the gas velocity is responsible for the momentum of the crown-shaped “corona” of the splashing shown in Fig. 1(a). Thus, this vertical component is essential for inducing corona splashing.

Fig. 14 compares a droplet at 100 kPa ambient pressure with the droplet at nearly a vacuum condition of 17.2 kPa. The slight deformation of the droplet due to the gas pressure is obvious in the experimental images. While it is difficult to see the qualitative difference in shape using the computational results, the quantitative difference is shown and discussed in the following figures. Due to viscous effects, the experimental deformation is greater than the BEM prediction; the gas cannot escape as readily in a

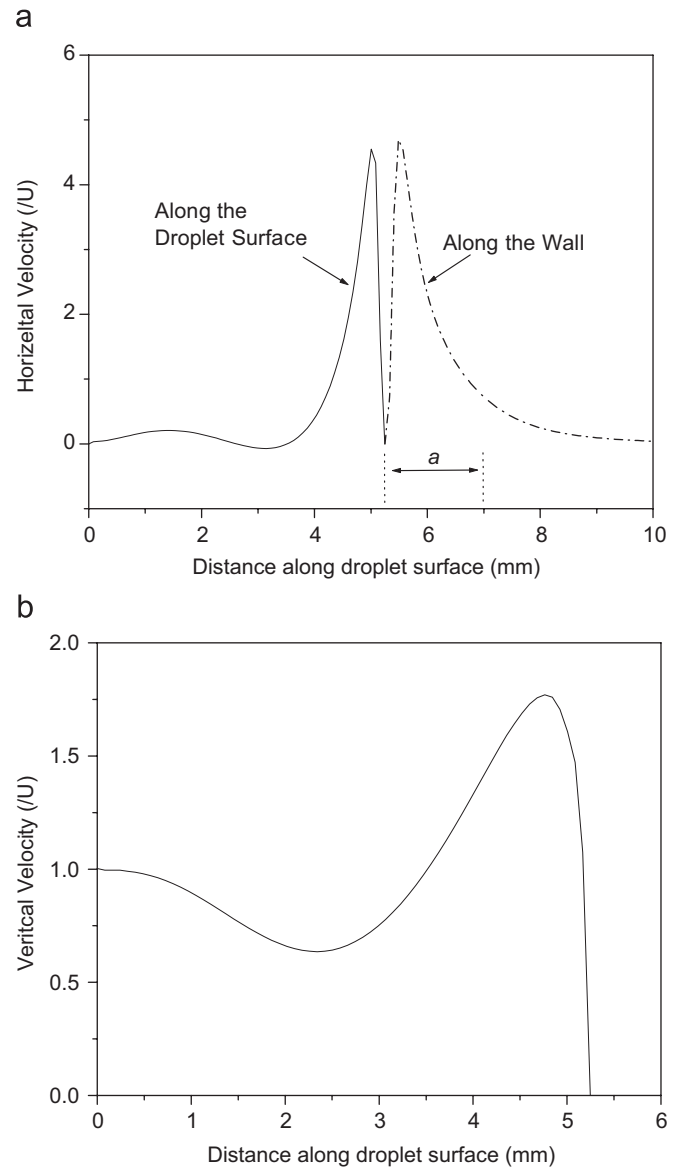


Fig. 13. The (a) horizontal and (b) vertical gas velocity profiles along the droplet surface of a falling droplet at the instance of impact under an ambient pressure condition.

viscous flow as in the BEM calculation, whose formulation is based on the inviscid flow.

3.4. Weber number effect

Fig. 15 shows the deformed droplet and its pressure distribution along the droplet’s surface at various Weber numbers. When the Weber number is relatively low (i.e., $We = 8.38$), nearly no deformation of the droplet can be observed as its data (represented by the “▲” symbol) overlap with those of the initial shape (see the dotted line in Fig. 15(a)). When the Weber number is relatively high (i.e., $We = 83,800$), the droplet is deformed in a similar manner as in the case of $We = 838$. These similar results indicate that the droplet’s shape is independent of the Weber

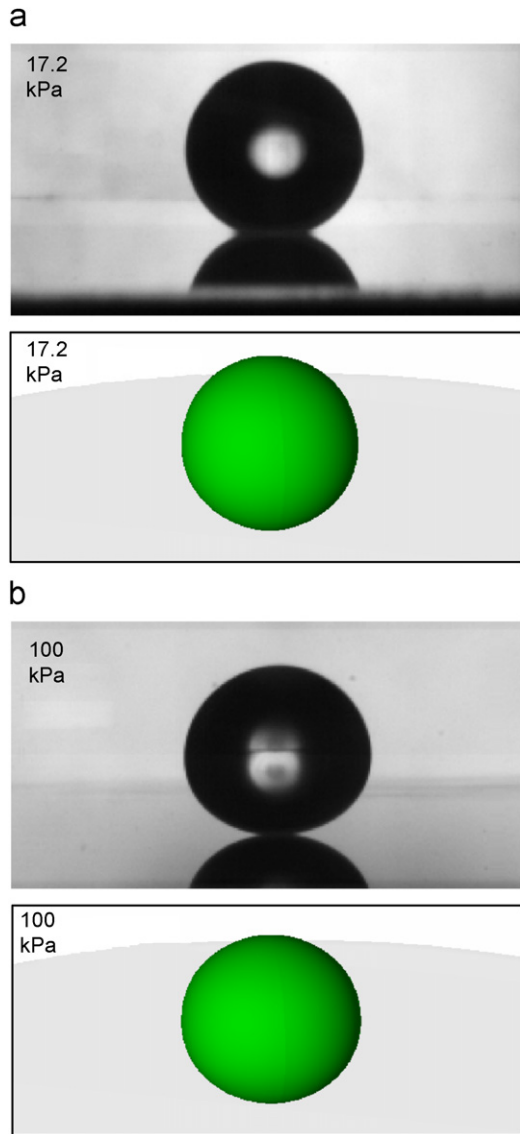


Fig. 14. The droplet shape comparison of a falling droplet at the instance of impact between (a) in the case of nearly vacuum condition and (b) the case of $P_{env} = 1\text{ atm}$ pressure condition. Experimental images are reprinted under the permission of Prof. Nagel of University of Chicago.

number when the Weber number exceeds a certain critical value. One may envision increasing the Weber number while increasing the impact speed (i.e., $We \propto U^2$) under the fixed values of droplet diameter and liquid properties. However, this dynamic pressure term does not contribute much to the total pressure (or stagnation pressure) at the bottom contact point of the falling droplet. For example, the total (or stagnation) pressure is $P_{env} + \rho_g U^2/2$ for an incompressible flow. When $P_{env} = 101\text{ kPa}$, it is difficult to produce a dynamic pressure comparable to the static pressure unless the droplet was traveling at a supersonic speed. For this reason, there was no droplet deformation observed with a moderate change in the Weber number as shown in Fig. 15(a). This result is consistent with the physical explanation mentioned above.

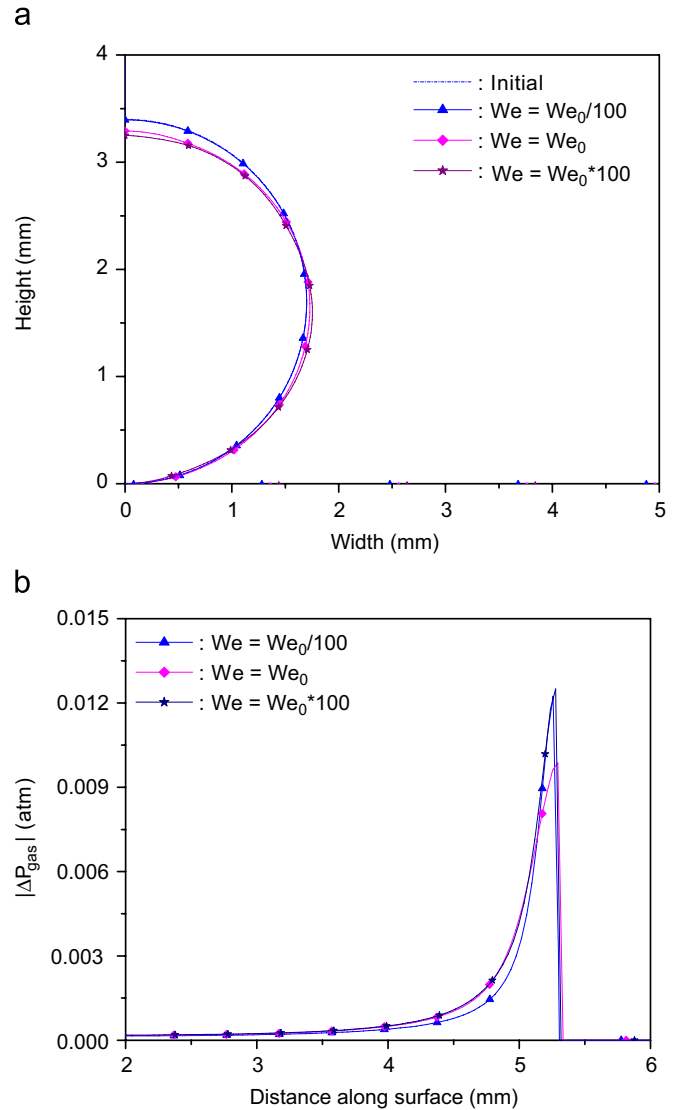


Fig. 15. The Weber number effect on (a) the droplet shape and (b) the pressure distribution along the droplet surface. Note that $We_0 = 838$.

3.5. Gas pressure effects

Fig. 16 shows the droplet deformation and the gas pressure distribution along the droplet surface at various P_{env} . As shown in Fig. 16(a), the droplet deforms with a greater curvature at a larger value of P_{env} as expected. We have shown computationally that the gas pressure is indeed important in inducing droplet deformation and, eventually, effects the droplet splash. This linear pattern of the increase in $|\Delta P_{gas}|$ is also interesting as its peak values reach approximately 0.013 atm and 0.025 atm at $P_{env} = 1\text{ atm}$ and 2 atm, respectively. This pattern indicates that a 1 atm increase in the ambient (or environmental) pressure results in about 1.3% increase in the stagnation gas pressure at the bottom contact point of the falling droplet. Using this linear relation, the peak value of the stagnation pressure at $P_{env} = 3\text{ atm}$ would be approximately $\sim 0.04\text{ atm}$ and would be $\sim 0.13\text{ atm}$ if $P_{env} = 10\text{ atm}$.

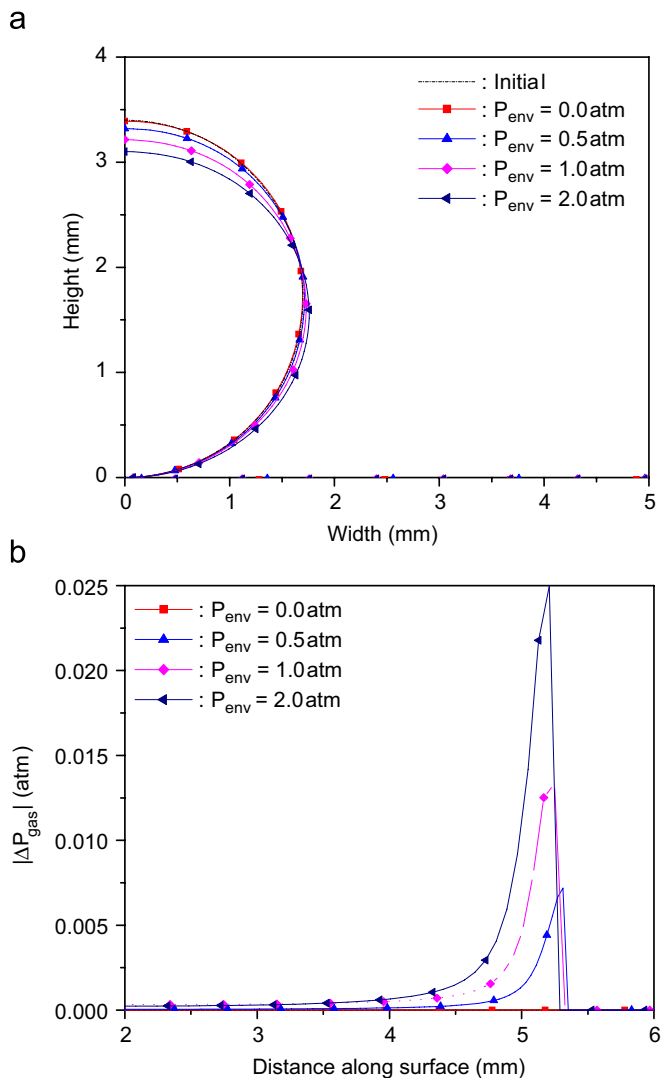


Fig. 16. The ambient gas pressure effect on (a) the droplet shape and (b) the pressure distribution along the droplet surface.

4. Conclusions

A BEM tool has been developed to study droplet impact and bouncing phenomena in the presence of a gaseous phase. The model has been shown to agree quite well with measured droplet deformations/topologies from a variety of experimental results. Droplet bouncing and small-scale capillary waves are resolved in the formulations that utilize linear elements in an axisymmetric context.

The effect of gas pressure on droplet deformation has been studied computationally. Moreover, droplet bounce was simulated for the case where the Weber number was relatively low such that the surface tension energy dominates over the dissipative energy of friction. The high escaping gas velocity, accelerated by the compression between the falling droplet and the stationary substrate wall, was also observed. The maximum velocity of the escaping gas reached nearly five times the impact speed, a result that was consistent with our experimental observa-

tion. It was also found that the peak stagnation gas pressure at the droplet's bottom during the time of impact has a linear relationship with the increasing atmospheric pressure.

Acknowledgements

The authors gratefully acknowledge the support of Sandia National Laboratories (SNL) under Grant No. LDRD05-0030. SNL is a multiprogram laboratory operated by Sandia Corporation, a Lockheed Martin Company for the United States Department of Energy's National Nuclear Security Administration under contract DE-AC04-94AL85000. The second author acknowledges his thanks for the partial support provided by Carbon Dioxide Reduction and Sequestration R;D Center (CDRS) of Korea.

References

- [1] Worthington AM. On the forms assumed by drops of liquids falling vertically on a horizontal plate. *Proc R Soc London A* 1876;25:261.
- [2] Worthington AM. A second paper on the forms assumed by drops of liquids falling vertically on a horizontal plate. *Proc R Soc London A* 1877;25:498.
- [3] Aziz SD, Chandra S. Impact, recoil and splashing of molten metal droplets. *Int J Heat Mass Transfer* 2000;43:2841–57.
- [4] Chandrasekhar S. *Hydrodynamic and Hydromagnetic Stability*. New York: Dover Publications Inc.; 1981.
- [5] Sivakumar D, Tropea C. Splashing impact of a spray onto a liquid film. *Phys Fluids* 2002;14:L85–8.
- [6] Xu L, Zhang W, Nagel SR. Drop splashing on a dry smooth surface. *Phys Rev Lett* 2005;94(18) No. 184505.
- [7] Allen RF. The role of surface tension in splashing. *J Colloid Interface Sci* 1975;51:350–1.
- [8] Trapaga G, Szekely J. Mathematical modeling of the isothermal impingement of liquid droplets in spraying processes. *Metall Trans B* 1991;22:901–14.
- [9] Trapaga G, Matthys EF, Valencia JJ, Szekely J. Fluid flow, heat transfer, and solidification of molten metal droplets impinging on substrates: comparison of numerical and experimental results. *Metall Trans B* 1992;23:701–18.
- [10] Liu HM, Lavernia EJ, Rangel RH. Numerical simulation of substrate impact and freezing of droplets in plasma spray processes. *J Phys D* 1993;26:1900–8.
- [11] Pasandideh-Fard M, Qiao YM, Chandra S, Mostaghimi J. Capillary effects during droplet impact on a solid surface. *Phys Fluids* 1996;8:650–9.
- [12] Foote GB. The water rebound problem: dynamics of collision. *J Atmos Sci* 1975;32:390–402.
- [13] Fukai J, Zhao Z, Poulikakos D, Megaridis CM, Miyatake O. Modeling of the deformation of a liquid droplet impinging upon a flat surface. *Phys Fluids A* 1993;5:2588–99.
- [14] Yarin AL, Weiss DA. Impact of drops on solid surfaces: self-similar capillary waves, and splashing as a new type of kinematic discontinuity. *J Fluid Mech* 1995;283:141–73.
- [15] Davidson MR. Boundary integral prediction of the spreading of an inviscid drop impacting on a solid surface. *Chem Eng Sci* 2000;55:1159–70.
- [16] Mao T, Kuhn CS, Tran H. Spread and rebound of liquid droplets upon impact on flat surfaces. *AIChE J* 1997;43:173–83.
- [17] Heister SD. Boundary element methods for two-fluid free surface flows. *Eng Anal Boundary Elem* 1997;19:309–17.

- [18] Spangler CA, Hilbing JH, Heister SD. Nonlinear modeling of jet atomization in the wind-induced regime. *Phys Fluids* 1995;7:964.
- [19] Gong SC. Spreading of droplets impacting on smooth solid surface. *Jpn J Appl Phys* 2005;44:3323–4.
- [20] Yoon SS, Jepsen RA, Nissen MR, O'Hern TJ. Experimental investigation on splashing and nonlinear fingerlike instability of large water drops. *J Fluids Struct* 2006;22:101–15.
- [21] Renardy Y, Popinet S, Duchemin L, Renardy M, Zaleski S, Josserand C, et al. Pyramidal and toroidal water drops after impact on a solid surface. *J Fluid Mech* 2003;484:69–83.
- [22] Jepsen RA, Yoon SS, Demosthenous B. Effects of air on splashing during a large droplet impact. *Atomization Sprays* 2006;16:1–16.